Chinese Chemical Letters 36 (2025) 109719

Contents lists available at ScienceDirect

Chinese Chemical Letters

journal homepage: www.elsevier.com/locate/cclet

Highly sensitive hydrazine detection through a novel Raman scattering quenching mechanism enabled by a crystalline and noble metal–free polyoxometalate substrate

Chunhui Zhang, Jie Wang, Jieyang Zhan, Runmin Yang, Guanggang Gao*, Jiayuan Zhang, Linlin Fan*, Mengqi Wang, Hong Liu*

School of Materials Science and Engineering, University of Jinan, Ji'nan 250022, China

ARTICLE INFO

Article history:
Received 12 December 2023
Revised 6 February 2024
Accepted 1 March 2024
Available online 11 March 2024

Keywords:
Polyoxometalate
Hydrazine
Raman detection
Quenching
Single crystal

ABSTRACT

In the field of Raman spectroscopy detection, the quest for a non–noble metal, recyclable, and highly sensitive detection substrate is of utmost importance. In this work, a new crystalline and noble metal–free substrate of $[Bi(DMF)_8][PMo_{12}O_{40}]$ (Bi–PMo_{12}) is designed, which is composed of $[PMo_{12}O_{40}]^{3-}$ and solvated $[Bi(DMF)_8]^{3+}$ cations. Mechanistic studies have revealed that Raman scattering quenching phenomenon arises from two main factors. Firstly, it arises from the absorption of the scattered light due to the transition of a single electron in the reduced state of Mo^V between 4d orbitals. Secondly, after the interaction between the substrate and hydrazine, the surface undergoes varying degrees of roughening, leading to an impact on the scattered light intensity. These two effects collectively contribute to the detection of low concentrations of N_2H_4. As a result, Bi–PMo_{12} opens up a novel Raman scattering quenching mechanism to realize the detection of reduced N_2H_4 small molecules. A remarkably low detection limit of 4.5×10^{-9} ppm for N_2H_4 is achieved on the Bi–PMo_{12} substrate. This detection has a lower concentration than the currently known SERS detection of N_2H_4. Moreover, Bi–PMo_{12} can be recovered and reused through recrystallization, achieving a recovery rate of up to *ca.* 51%. This study reveals the underlying potential of crystalline polyoxometalate materials in the field of Raman detection, thus opening up new avenues for highly sensitive analysis using Raman techniques.

Hydrazine (N_2H_4) is a carcinogenic substance that induces pathological alterations in cells [1]. Moreover, its N_2H_4 vapor or liquid can be absorbed into the body through the respiratory tract, gastrointestinal tract, or skin, leading to central nervous system disorders, dermatitis, and permanent eye damage [2,3]. Despite its adverse effects, it remains an indispensable constituent in the aerospace and chemical sectors [4]. With the development of industry, the widespread use of N_2H_4 has posed potential risks to human health and environmental safety [5]. The United States Environmental Protection Agency (EPA) mandates that its concentration in water should not exceed 10 parts per billion (ppb) [6]. Indeed, a range of detection methods has been developed for trace analysis of N_2H_4. These methods primarily include fluorescence analysis [7,8], electrochemical analysis [9,10], colorimetry [11], and so on. Although the above–mentioned methods demonstrate satisfactory detection performance, there are still limitations in the detection of gaseous N_2H_4.

Raman spectroscopy is widely recognized as a highly powerful detection technique, distinguished by its non–destructive and non–invasive nature, as well as its relatively straightforward operational procedures [12–16]. When a beam of light illuminates a sample, a small portion of the incident light undergoes wavelength shifts due to the sample's structural characteristics [17]. This phenomenon is known as Raman scattering effect. However, Raman scattering, inherently possessing weak scattering characteristics, cannot be utilized for trace analysis during its initial discovery until the emergence of Surface–enhanced Raman spectroscopy (SERS) [18–22]. In recent years, SERS spectroscopy has been widely used for the detection of many small molecular substances [23–27]. There are also some applications in the detection of N_2H_4, which exhibit excellent performance [28–30]. However, in most instances, noble metals are incorporated into Raman substrates utilized for SERS detection. Indeed, this specific substrate not only comes with a significant cost but also demonstrates a permanent decrease in surface–enhanced Raman scattering (SERS) activity when its surface structure under-

* Corresponding authors.
E-mail addresses: mse_gaogg@ujn.edu.cn (G. Gao), mse_fanll@ujn.edu.cn (L. Fan), mse_liuh@ujn.edu.cn (H. Liu).

https://doi.org/10.1016/j.cclet.2024.109719
1001-8417/

goes alterations. As a consequence, the cost of detection experiences a significant surge [31,32]. Currently, the investigation into recyclable non–noble metal Raman substrates for the detection of low–concentration N_2H_4 poses a significant challenge in the field of research.

Polyoxometalates (POMs) are typically metal oxide clusters [33–41]. POMs contain a significant number of metal–oxygen bonds [42–53], and the stretching vibration of these metal–oxygen bonds exhibits pronounced Raman signals [54–56]. Moreover, POMs possess a high surface charge, which can attract cations from the solution and form new compounds that precipitate in the form of crystals [57]. These well–defined crystalline POMs materials further amplify the Raman signals of the metal–oxygen bonds, resulting in strong Raman signals. In addition, since the transition metals in POMs are in their highest oxidation states, they can be easily reduced by reducing agents, leading to the formation of metal centers with single electrons [58]. These metal centers may induce lattice defects, thereby weakening the Raman signals [59]. In light of the inherent reversibility of the oxidation-–reduction process of POMs, the reduced form of POMs can be efficiently regenerated to its oxidized state in the presence of an oxidizing agent [60]. Utilizing the oxidation-reduction mechanism of crystalline POMs holds the potential for achieving repeated utilization of substrate materials. Furthermore, research has demonstrated that certain stable, solvated metal cations (such as Pb^{2+}, Bi^{3+}, and Ln^{3+}, among others) have been found to efficiently form crystalline materials with polyoxometalates through electrostatic attraction [61,62]. These materials exhibit excellent stability and facilitate the reduction of metal centers in the polyoxometalate framework [63]. However, to date, only the photochromic properties of such materials have been extensively studied, while their detection capabilities and potential applications in the field of Raman sensing remain unexplored.

In this study, a single crystal compound of $[Bi(DMF)_8]PMo_{12}O_{40}$ ($Bi–PMo_{12}$) is designed and synthesized by simple conventional solution method. Through the utilization of $Bi–PMo_{12}$ as a Raman substrate and the presence of N_2H_4 gas, the Mo^{VI} ions within the POMs anions can be effectively reduced to Mo^{V} centers. Simultaneously, the intensity of Raman signals weakens with increasing concentrations of N_2H_4, allowing for the detection of N_2H_4 vapor. The detection range spans from 4.5×10^1 ppm to 4.5×10^{-9} ppm. In addition, during the detection process, it is also observed for the first time that the surface of the $Bi\text{-}PMo_{12}$ crystal changes from smooth to rough upon exposure to N_2H_4 vapor. This surface etching also contributes to the quenching of the Raman signals, further assisting in the detection process. Moreover, following the detection process, $Bi\text{-}PMo_{12}$ can undergo recrystallization in a solution of *N*,*N*-dimethylformamide (DMF) containing H_2O_2, thereby enabling the cyclic utilization of the substrate materials.

In previous studies, DMF has been found to significantly enhance the reduction ability of POMs, resulting in an amplified signal response for light intensity detection [64]. In this work, to enhance the redox capacity of POMs and achieve the goal of N_2H_4 detection, it is desirable to incorporate a greater number of DMF molecules into the system, by utilizing Bi^{3+}, a metal ion with a high coordination number. During the experimental process, a straightforward and conventional approach involving room temperature stirring and diffusion-induced crystallization was employed. By utilizing this method, a solvent-assisted POMs, $Bi\text{-}PMo_{12}$, was successfully synthesized with an approximate yield of 30% (based on Mo). Comparatively, the synthesis method for $Bi\text{-}PMo_{12}$ is simpler and more cost-effective than that of other noble metal substrates.

The X-ray single crystal structure analysis reveals that $Bi\text{-}PMo_{12}$ belongs to the triclinic crystal system with the $P\bar{1}$ space group (Table S1 in Supporting information). It is composed of $[PMo_{12}O_{40}]^{3-}$ and $[Bi(DMF)_8]^{3+}$ units (Fig. 1a). $[PMo_{12}O_{40}]^{3-}$ is a typical Keggin-type POMs [65]. In $[Bi(DMF)_8]^{3+}$, eight solvent molecules DMF act as monodentate ligands, coordinating with the central Bi^{3+} and forming a commonly observed eight-coordinate square antiprismatic geometry. The $[Bi(DMF)_8]^{3+}$ cation readily forms crystals with the $[PMo_{12}O_{40}]^{3-}$ anion in solution, exhibiting a 1:1 ratio (Fig. 1b). Fig. S1 (Supporting information) shows the morphology of dried $Bi\text{-}PMo_{12}$, indicating the relative stability of the crystalline structure after drying. The experimental X-ray powder diffraction (XRD) data of $Bi\text{-}PMo_{12}$ is consistent with the fitting data of its single crystal phase (Fig. 1c).

Analysis of the Fourier–transform infrared spectroscopy (FTIR) of $Bi–PMo_{12}$ reveals characteristic peaks at 1060 cm^{-1} to 798 cm^{-1} (Fig. 1d), corresponding to $H_3PMo_{12}O_{40}{\cdot}4H_2O$ (H_3PMo_{12}), and a peak at 1651 cm^{-1} and 1350 cm^{-1} corresponding to the C=O stretching vibration of DMF [64,66]. Fig. 1e displays the Raman spectra of $Bi–PMo_{12}$ and H_3PMo_{12} under 532 nm laser wavelength. The characteristic absorption peaks at 887 cm^{-1}, and 987 cm^{-1} correspond to the symmetric and antisymmetric stretching vibrations of the Mo=O bonds [67]. As shown in Fig. 1f, the scanning electron microscopy (SEM) image of $Bi–PMo_{12}$ reveals that even after grinding, the crystal facets remain intact. Although some surface cracks are visible, within the laser spot area (1 μm), the surface remains smooth and intact, ensuring the stability of the output Raman signals. The clear element distribution of P, Mo, Bi, and N in $Bi–PMo_{12}$ can be observed in Fig. 1g. The uniform distribution of these elements further confirms the successful synthesis of $Bi–PMo_{12}$.

We explore the parameters that may affect the detection results of N_2H_4 in order to obtain the optimal testing conditions for $Bi–PMo_{12}$. As shown in Figs. S2 and S3 (Supporting information), stable Raman signals can be obtained at a laser intensity of 25% and a sampling time of 4 s. Moreover, by heating the sample, it can be observed from the Raman spectra that the Raman signal of $Bi–PMo_{12}$ remains unchanged until 70 °C and undergoes quenching at 80 °C (Fig. S4 in Supporting information). This phenomenon can be attributed to the reduction of $Bi–PMo_{12}$ induced by a small quantity of volatile DMF (Fig. S5 in Supporting information). As illustrated in Fig. S6 (Supporting information), the relative humidity has no impact on the Raman signal intensity of $Bi–PMo_{12}$, regardless of the presence of N_2H_4 at a concentration of 4.5×10^{-9} ppm (Figs. S6a and b) or its absence (Figs. S6c and d). Subsequently, ten random points on $Bi–PMo_{12}$ substrate were selected for Raman testing, and it was observed that the Raman signals exhibited a uniform distribution across these points (Fig. S7a in Supporting information). Fig. S7b (Supporting information) showcases the histogram of Raman signal intensities at 987 cm^{-1} (I_{987}), revealing an impressively low relative standard deviation (RSD) of merely 1.06%. This strongly indicates the remarkable stability of the $Bi–PMo_{12}$ substrate.

Based on these findings, it can be concluded that the quenching effect of the Raman signal is optimized at a reaction temperature of 70 °C and a reaction time of 30 min (Fig. 2a). It is evident from the obtained spectra that the intensity of Raman signals exhibits a quenching trend with the increasing concentration of N_2H_4 (Fig. 2b). Furthermore, it can be observed from the blue line in Fig. 2c that there is a trend in the change of I_{987} with the logarithm of N_2H_4 concentration ($\lg(C_{N_2H_4})$). The linear correlation coefficient (R^2) is 0.9978. The logarithm of the N_2H_4 concentration is inversely proportional to I_{987} within the concentration range of 4.5×10^1 ppm to 4.5×10^{-9} ppm. The equation representing this relationship is: $y = 206.62206 - 101.27295x$ (y represents the intensity of I_{987}, and x represents $\lg(C_{N_2H_4})$). In the detection of N_2H_4, $Bi–PMo_{12}$ can realize the detection at least 4.5×10^{-9} ppm. As shown in Table S2 (Supporting information), the results obtained in this study are superior to other meth-

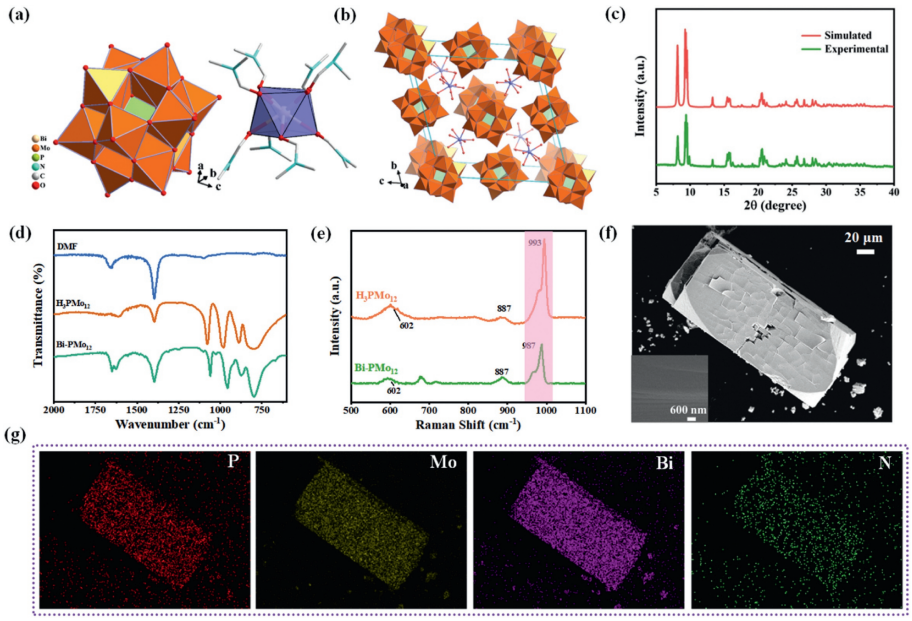

Fig. 1. (a) The crystal structure diagram and (b) single unit cell illustration of Bi–PMo_{12}. (c) The XRD patterns of Bi–PMo_{12}. (d) FTIR and (e) Raman spectra of Bi–PMo_{12} and H_3PMo_{12} respectively. (f) SEM and (g) the element mapping images of P, Mo, Bi, and N of Bi–PMo_{12}.

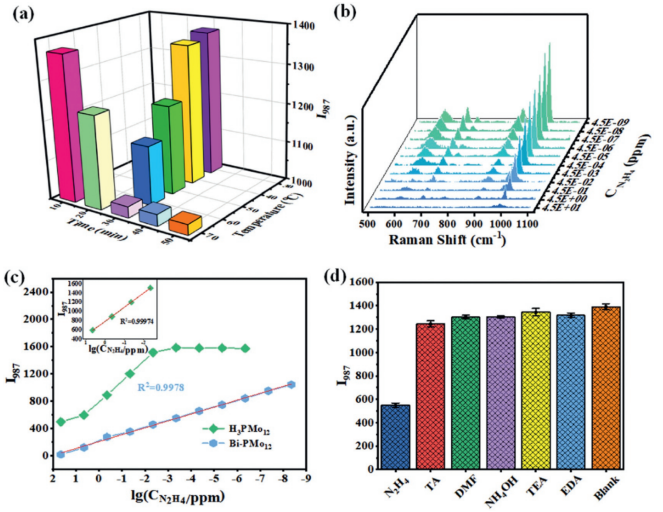

Fig. 2. (a) The histogram of Raman signal intensities at 987 cm^{-1} of Bi–PMo_{12} in 4.5×10^{-9} ppm N_2H_4 at different temperatures and times. (b) Raman spectra of Bi–PMo_{12} after reaction with different concentrations of N_2H_4 (4.5×10^{1}–4.5×10^{-9} ppm). (c) The correlation curve between the logarithm of N_2H_4 concentration ($lg(C_{N_2H_4})$, $C_{N_2H_4}$ represents the concentration of the N_2H_4 vapor) of Bi–PMo_{12} and H_3PMo_{12} at 987 cm^{-1} strength. (d) The histogram of Raman signal intensity of Bi–PMo_{12} at 987 cm^{-1} in the presence of N_2H_4 (4.5×10^{-4} ppm) and other reducing compounds (4.5×10^{-2} ppm), respectively. The error bar is obtained at least three replicate trials.

ods for detecting N_2H_4. The results of the new method surpass the effectiveness of SERS detection of N_2H_4, providing a novel approach for the detection of low–concentration reducing gases. Furthermore, when the concentration of N_2H_4 is 4.5×10^{-9} ppm and 4.5×10^{-1} ppm, the Raman signal intensity at 987 cm^{-1} is similar for the three different samples, exhibiting good reproducibility (Fig. S8 in Supporting information). Furthermore, in the presence of 4.5 ppm N_2H_4, the observed variation in I_{987} values at 10 randomly selected points is minimal, with a relatively low standard RSD value of 1.71% (Fig. S9 in Supporting information). In addition, it was discovered that H_3PMo_{12} also exhibited Raman quenching behavior under N_2H_4 atmosphere (Fig. 2c and Fig. S10 in Supporting information). The Raman quenching effect of H_3PMo_{12} was optimized under the conditions of 70 °C and 30 min (Fig. S11 in Supporting information). However, the detection concentration range only attains at 4.5×10^{1}–4.5×10^{-3} ppm. This finding suggests that the presence of $[Bi(DMF)_8]^{3+}$ cations significantly enhances the detection performance of Bi–PMo_{12}, thus playing a crucial role in achieving effective detection at low concentrations.

To showcase the interference resistance capability of Bi–PMo_{12}, we conducted parallel tests on several amine compounds (4.5×10^{-2} ppm), which have the potential to cause interference. The purpose of these tests was to evaluate the selectivity of Bi–PMo_{12} in detecting N_2H_4 (4.5×10^{-4} ppm). As depicted in Fig. 2d, although a quenching effect was observed in the presence of triethylamine (TA), N,N–dimethylformamide (DMF), ammonium hydroxide (NH_4OH), trolamine (TEA), and ethylenediamine (EDA) atmospheres, it was more pronounced in the presence of N_2H_4. Compared to other amine compounds, the I_{987} value decreases by over 60.56% in the presence of N_2H_4. And compared to the blank, other amine compounds only show a decrease of approximately 6.32% in the I_{987} value. Therefore, Bi–PMo_{12} exhibits excellent selectivity for N_2H_4 detection. This exceptional selectivity can be attributed to the limited ability of other low–concentration amine compounds to effectively reduce Bi–PMo_{12}.

The FTIR and Raman spectra of Bi–PMo_{12} before and after detection indicate that there is no change in the molecular structure of Bi–PMo_{12} (Figs. 3a and b). It is consistent with the conclusion that the structure of POMs remains unchanged after receiving electrons [68]. As shown in Fig. 3c, the X–ray photoelectron spectroscopy (XPS) characteristic peaks for Mo 3d are observed at 236.15, 232.98, 234.93, and 231.77 eV, indicating the presence of Mo^{VI} $3d_{3/2}$, Mo^{VI} $3d_{5/2}$, Mo^{V} $3d_{3/2}$, and Mo^{V} $3d_{5/2}$. After treatment with N_2H_4 at concentrations of 4.5×10^{-4} ppm and 4.5 ppm respectively, the peak area corresponding to Mo^{V} increased from 23.43% to 31.22% and 38.32%, respectively. This can be attributed to that Mo^{VI} in Bi–PMo_{12} undergoes partial reduction. It should be noted that the appearance of Mo^{V} in Bi–PMo_{12} prior to detection is mainly due to the influence of X–ray in XPS testing, while

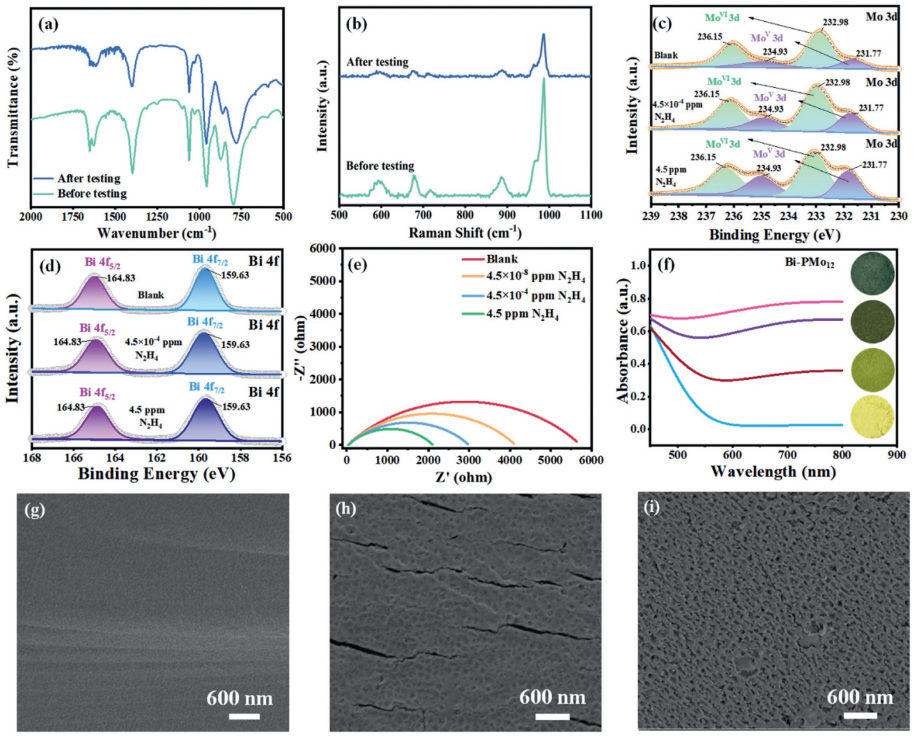

Fig. 3. (a) Comparison of FTIR and (b) Raman spectra of Bi–PMo_{12} before and after detection of N_2H_4. XPS analysis of (c) Mo 3d and (d) Bi 4f spectra of Bi–PMo_{12} before and after reduction by 4.5×10^{-4} ppm and 4.5 ppm N_2H_4. (e) Nyquist plots of Bi–PMo_{12} in the presence of N_2H_4. (f) UV–vis diffuse reflectance spectra (left) and colour changes (right) of Bi–PMo_{12} with different concentrations of N_2H_4. The surface analysis of Bi–PMo_{12} (g) before and (h, i) after reduction with N_2H_4 (4.5×10^{-4} ppm and 4.5 ppm).

weaker laser and lower frequency light do not have this effect. Furthermore, there was no change observed in the Bi, O, P, and N elements after the N_2H_4 treatment (Fig. 3d and Fig. S12 in Supporting information).

Previous studies have demonstrated that the reduction of Mo^{VI} generates Mo^{V} species with hole–lone electron pairs, resulting in increased conductivity and decreased impedance [64]. As shown in Fig. 3e, after the N_2H_4 treatment, the impedance values of Bi–PMo_{12} gradually decrease, indicating the generation of Mo^{V} species. Moreover, as depicted in Fig. 3f, the color of Bi–PMo_{12} gradually deepens with increasing concentrations of N_2H_4 treatment, accompanied by a corresponding increase in the absorbance values within the range of 530–800 nm in the solid–state diffuse reflectance spectra (UV–vis). Specifically, the absorbance values at 710 nm exhibit an increase from 0.0234 (without N_2H_4 treatment) to 0.7729 (with 4.5 ppm N_2H_4 treatment). This analysis indicates that the single–electron transitions occurring between different d orbitals on the Mo^{V} centers of the reduced Bi–PMo_{12} can efficiently absorb the Raman scattering irradiation, thereby resulting in the quenching of the Raman signals. As such, we propose to denominate this a new effect as Raman resonance energy transfer (RRET). By harnessing this novel RRET effect, more stable and highly active Raman sensing substrates can be skillfully engineered, enabling their efficacious detection of diverse reducible small molecules.

Fig. 3g demonstrates the surface morphology of Bi–PMo_{12} prior to N_2H_4 reduction, revealing a smooth surface with well–defined crystal planes within the laser spot area (1 μm) and no discernible defects. The surface characterization of Bi–PMo_{12} subsequent to treatment with N_2H_4 (4.5×10^{-4} and 4.5 ppm) was examined (Figs. 3h and i), revealing that an escalation in N_2H_4 concentration led to enhanced surface etching of Bi–PMo_{12} and increased depth of surface pores. Moreover, the surface pores of Bi–PMo_{12} after N_2H_4 treatment exhibit remarkable uniformity, which is a crucial aspect for maintaining stable Raman signals. It can

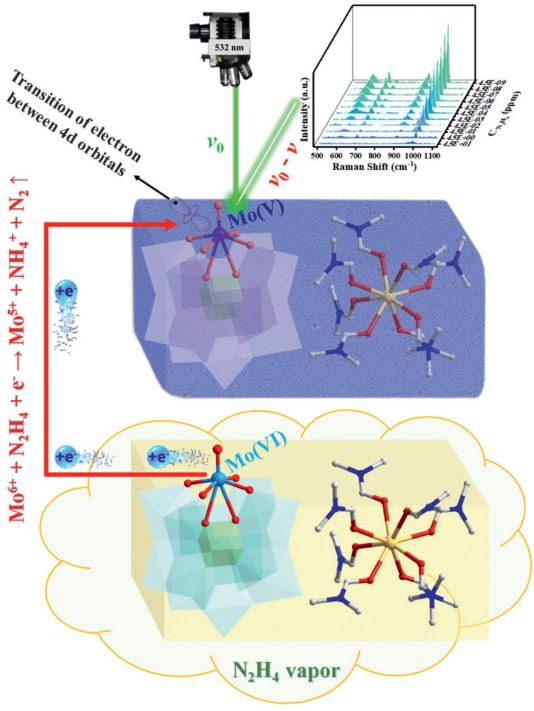

Fig. 4. Proposed mechanism for the Raman detection of N_2H_4 by the Bi–PMo_{12} substrate.

be speculated that this surface modification may represent an additional factor contributing to the attenuation of the Raman signals. To substantiate this proposition, an analysis of the morphology of H_3PMo_{12} after the detection of equimolar concentration of N_2H_4 was also conducted. The results indicate that the surface of

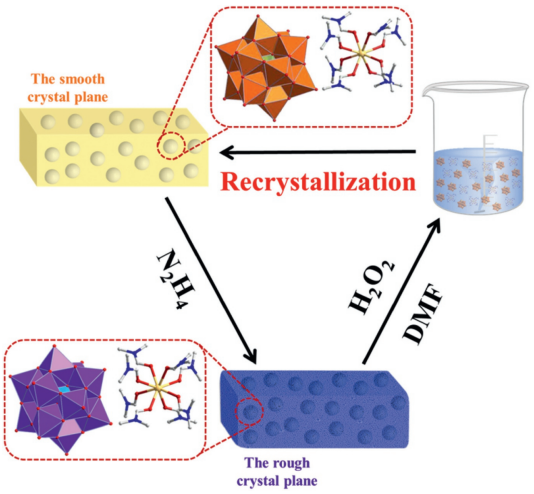

Fig. 5. Schematic diagram of recycling process for Bi–PMo_{12}.

H_3PMo_{12} is smooth (Fig. S13a in Supporting information) and similar to Bi–PMo_{12}, showing no apparent defects within the laser spot range before N_2H_4 treatment. After treatment with 4.5 ppm N_2H_4 (Fig. S13b in Supporting information), H_3PMo_{12} exhibited some degree of surface weathering, but did not show uniform pore formation like Bi–PMo_{12}. This change will not increase the diffuse reflection of light. This aligns with the experimental findings, confirming that the surface alteration of Bi–PMo_{12} is also contributable to the attenuation of Raman signals.

Based on the aforementioned analyses, we can propose the following reasonable detection mechanism for Bi–PMo_{12} as depicted in Fig. 4. During the reaction, Mo^{VI} in POMs is reduced to Mo^{V}, filling unsTable 4d orbitals. These d–d orbital transitions absorb energy from Raman scattering, resulting in a substantial reduction in signal output. On the other hand, in the presence of a N_2H_4 atmosphere, DMF efficiently captures gaseous N_2H_4 molecules from the surrounding environment, facilitating close contact between gaseous N_2H_4 and the crystal facets of Bi–PMo_{12}. The adsorbed N_2H_4 induces uniform pore defects on the surface of Bi–PMo_{12}, enhancing the diffuse reflection of light. The aforementioned synergistic effects of these two actions ultimately led to the quenching behavior of Raman scattering signals, thereby enabling highly sensitive detection of N_2H_4.

During the experimental process, we observed that Bi–PMo_{12} crystals could be recrystallized in DMF (Fig. 5). By introducing a small quantity of H_2O_2 into DMF solution of Bi–PMo_{12}, the Bi–PMo_{12} compound undergoes reoxidation. Subsequently, this solution is subjected to diffusion crystallization in ethanol, resulting in the crystallization of recrystallized Bi–PMo_{12} (r–Bi–PMo_{12}). The recovery rate reaches 51%.

FTIR spectra and XRD patterns show that the molecular structure of r–Bi–PMo_{12} remains unchanged, with characteristic peaks of $[PMo_{12}O_{40}]^{3-}$ and DMF appearing at 1060–798 cm^{-1} and 1651 cm^{-1}, respectively. XRD patterns demonstrate no alteration in the characteristic diffraction peaks of $[PMo_{12}O_{40}]^{3-}$ at 8.28°, 8.90°, 9.10°, and 27.9° (Figs. 6a and b). Further confirmation was obtained that Bi–PMo_{12} and r–Bi–PMo_{12} have the same crystal structure. As shown in Fig. 6c, the XPS spectrum of Mo 3d reveals a noticeable decrease in the peak area of Mo^{V} from 38.32% to 18.41%, demonstrating the successful oxidation of Mo^{V} to Mo^{VI} by H_2O_2. Furthermore, SEM testing was conducted on the surface of the reprecipitated r–Bi–PMo_{12} crystals from DMF (Fig. 6d). On the resulted surface, the r–Bi–PMo_{12} surface is restored to a smooth state, and the influence of N_2H_4 on its surface disappears (illustration of Fig. 6d). From Figs. 6e–h, it can be observed that r–Bi–PMo_{12} maintains its Raman signal quenching properties during the four cycles. Furthermore, it can be observed from Fig. 6i that

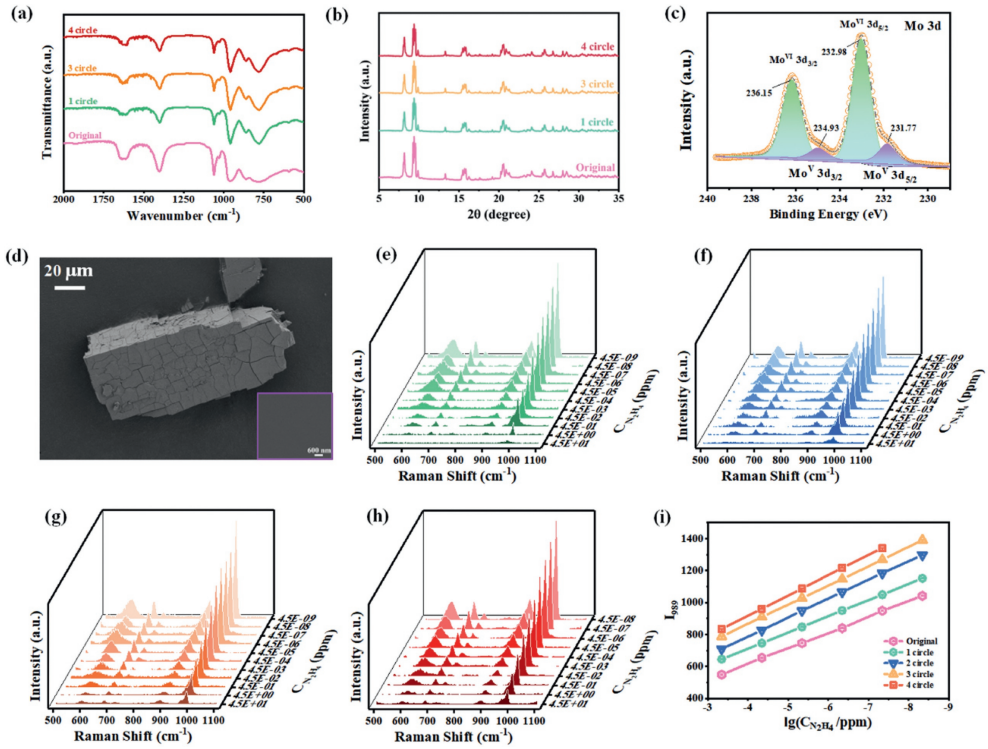

Fig. 6. (a) Comparative FTIR and (b) Raman spectra of Bi–PMo_{12} with different cycles. (c) XPS analysis of r–Bi–PMo_{12} for Mo 3d spectra. (d) SEM image characterization of r–Bi–PMo_{12}. Raman spectra of r–Bi–PMo_{12} after reaction with different concentrations of N_2H_4 (4.5×10^{1}–4.5×10^{-9} ppm): (e) First cycle; (f) second cycle, (g) third cycle and (h) fourth cycle. (i) The correlation curve between the $lg(C_{N_2H_4})$ of r–Bi–PMo_{12} and the strength at 987 cm^{-1}.

the Raman signal intensity at 987 cm^{-1} still exhibits a linear relationship with the lg(CN_2H_4) with similar slopes. However, it can be observed that due to the oxidizing effect of H_2O_2, the amount of Mo^{VI} increases, resulting in a stronger initial Raman signal of r–Bi–PMo_{12}. The fourth attempt to measure the concentration of N_2H_4 only reached a limit of 4.5×10^{-8} ppm. Nevertheless, even after four cycles, the detection capability of Bi–PMo_{12} remains comparable to the reported SERS technique [28–30]. Therefore, the Bi–PMo_{12} crystalline substrate exhibits exceptional recyclability and serves as an excellent substrate for Raman detection.

In this study, a novel crystalline Raman substrate, Bi–PMo_{12}, free of noble metals, was successfully designed and synthesized. It demonstrates exceptional detection capabilities for N_2H_4, with a detection limit as low as 4.5×10^{-9} ppm, surpassing even the performance of the SERS technique. Through the exploration of detection mechanism, a novel RRET effect based on the absorption of Raman scattered light by reduced POMs was discovered for the first time. Simultaneously, solvation of cations during the detection process played a crucial role in the adsorption of the target molecules, inducing quenching of the substrate's Raman signals. The discovery of these two effects provides important guidance for the design and synthesis of non–noble metal Raman detection substrates, enabling the development of more Raman detection substrates based on crystalline POMs materials. This study will significantly accelerate the rapid progress of highly active non–noble metal Raman detection substrates in the domain of toxic gas detection.

Declaration of competing interest

The authors declare that they have no known competing financial interests or personal relationships that could have appeared to influence the work reported in this paper.

Acknowledgments

The authors gratefully acknowledge the financial support from the National Natural Science Foundation of China (No. 21971085) and the Natural Science Foundation of Shandong Province (No. ZR2021MB008).

Supplementary materials

Supplementary material associated with this article can be found, in the online version, at doi:10.1016/j.cclet.2024.109719.

References

[1] X.D. Jin, C.Z. Liu, X.M. Wang, et al., Sens. Actuator. B: Chem. 216 (2015) 141–149.
[2] S. Erdemir, S. Malkondu, M. Oguz, Chem. Eng. J. 468 (2023) 143767.
[3] M.G. Teng, Z.X. Zhou, Y.M. Qin, et al., Sens. Actuator. B: Chem. 311 (2020) 127914.
[4] P.C. Wang, Y.C. Liao, Y.L. Lai, et al., Carbon 50 (2012) 1650–1658.
[5] B. Garg, T. Bisht, Y.C. Ling, Spectrochim. Acta A Mol. Biomol. Spectrosc. 251 (2021) 119456.
[6] P. Ji, J.Y. Li, W.S. Wang, et al., Spectrochim. Acta A Mol. Biomol. Spectrosc. 293 (2023) 122492.
[7] B.B. Wang, R.J. Yang, W. Zhao, J. Hazard. Mater. 406 (2021) 124589.
[8] P. Liu, W.N. Wu, Y. Wang, Y.C. Fan, Z.H. Xu, J. Hazard. Mater. 440 (2022) 129713.
[9] J.P. Liu, Y.Y. Li, J. Jiang, X.T. Huang, Dalton Trans. 39 (2010) 8693–8697.
[10] I.V. Bagal, A. Ejaz, A. Waseem, et al., ACS Appl. Nano Mater. 3 (2020) 4394–4406.
[11] K. Zuo, J. Zhang, L.T. Zeng, Spectrochim. Acta A Mol. Biomol. Spectrosc. 283 (2022) 121765.
[12] Y.Y. Lu, X. Zhang, L.Y. Zhao, et al., Nat. Commun. 14 (2023) 5860.
[13] C. Hanske, E.H. Hill, D. Vila–Liarte, et al., ACS Appl. Mater. Interfaces 11 (2019) 11763–11771.
[14] L.Y. Bi, H.R.C. Zhang, W.C. Hu, et al., Biosens. Bioelectron. 237 (2023) 115519.
[15] H.H. Li, M.M. Hassan, J.J. Wang, et al., Food Chem. 339 (2021) 127843.
[16] Y.H. Wang, S.N. Li, R.Y. Zhou, et al., Nat. Protoc. 18 (2023) 883–901.
[17] H.L. Liu, K. Zhan, K. Wang, X.H. Xia, Trends Anal. Chem. 159 (2023) 116939.
[18] S.E.J. Bell, G. Charron, E. Cortés, et al., Angew. Chem. Int. Ed. 59 (2020) 5454–5462.
[19] T. Itoh, M. Procházka, Z.C. Dong, et al., Chem. Rev. 123 (2023) 1552–1634.
[20] S. Cong, Y.Y. Yuan, Z.G. Chen, et al., Nat. Commun. 6 (2015) 7800.
[21] J.Q. Zhao, J.H. Wang, Y.W. Liu, et al., Biosens. Bioelectron. 216 (2022) 114660.
[22] Y.W. Liu, H. Ma, X.X. Han, B. Zhao, Mater. Horizon. 8 (2021) 370–382.
[23] S. Cong, Z. Wang, W.B. Gong, et al., Nat. Commun. 10 (2019) 678.
[24] S. Schlücker, Angew. Chem. Int. Ed. 53 (2014) 4756–4795.
[25] J. Wang, W.J. Zhu, J.Y. Zhang, et al., Sens. Actuator. B: Chem. 381 (2023) 133450.
[26] C. Peng, L.L. Jin, F. Wang, H.F. Yang, H.Y. He, Biosens. Bioelectron. 225 (2023) 115079.
[27] S.E.J. Bell, N.M.S. Sirimuthu, J. Am. Chem. Soc. 128 (2006) 15580–15581.
[28] G.D. Xu, N. Guo, Q.J. Zhang, et al., J. Hazard. Mater. 424 (2022) 127303.
[29] J. Wang, J.Y. Zhang, W.J. Zhu, et al., J. Mater. Chem. C 11 (2023) 3050–3058.
[30] X. Gu, J.P. Camden, Anal. Chem. 87 (2015) 6460–6464.
[31] M. Shafi, P.Y. Duan, W.Y. Liu, et al., Sens. Actuator. B: Chem. 380 (2023) 133410.
[32] H. Fang, C.X. Zhang, L. Liu, Y.M. Zhao, H.J. Xu, Biosens. Bioelectron. 64 (2015) 434–441.
[33] J. Song, Y.Y. Jiang, Y.Z. Lu, et al., Small 19 (2023) 2301740.
[34] K.J. Qin, D.J. Zang, Y.G. Wei, Chin. Chem. Lett. 34 (2023) 107999.
[35] L. Guo, L. He, Q.H. Zhuang, et al., Small 19 (2023) 2207315.
[36] S.M. Zhang, W.X. Shi, X. Wang, Science 377 (2022) 100–104.
[37] J.X. Liu, X.B. Zhang, Y.L. Li, S.L. Huang, G.Y. Yang, Coord. Chem. Rev. 414 (2020) 213260.
[38] Y. Guan, H.P. Xiao, X.X. Li, S.T. Zheng, Polyoxometalates 2 (2023) 9140023.
[39] X.X. Li, C.H. Li, M.J. Hou, et al., Nat. Commun. 14 (2023) 5025.
[40] J. Liu, N. Jiang, J.M. Lin, et al., Angew. Chem. Int. Ed. 62 (2023) e202304728.
[41] B. Li, W. Li, H.L. Li, L.X. Wu, Acc. Chem. Res. 50 (2017) 1391–1399.
[42] C. Wang, Z.X. Gao, H.Y. Zang, T.W. Dong, Z.M. Su, Inorg. Chem. Front. 10 (2023) 3641–3647.
[43] H.Y. Zhang, D.Y. Cui, T.Y. Shen, et al., ACS Appl. Mater. Interfaces 15 (2023) 32281–32290.
[44] F.R. Li, H.R. Liu, W.C. Chen, et al., Inorg. Chem. Front. 9 (2022) 3828–3838.
[45] Q.D. Liu, H.D. Yu, Q.H. Zhang, D. Wang, X. Wang, Adv. Funct. Mater. 31 (2021) 2103561.
[46] T.T. Zhao, N.L. Bell, G. Chisholm, et al., Energ. Environ. Sci. 16 (2023) 2603–2610.
[47] Y. Yang, Y.M. Fu, Y.R. Tian, et al., Inorg. Chem. Front. 10 (2023) 6221–6228.
[48] Y.F. Liu, G.D. Zeng, Y.T. Cheng, et al., Chin. Chem. Lett. 35 (2024) 108480.
[49] K.T. Zheng, B.X. Niu, C.M. Lin, et al., Chin. Chem. Lett. 34 (2023) 107238.
[50] H.Q. Yin, L.L. Yang, H. Sun, et al., Chin. Chem. Lett. 34 (2023) 107337.
[51] G.P. Yang, K. Li, C.W. Hu, Inorg. Chem. Front. 9 (2022) 5408–5433.
[52] L.L. Fan, M.L. Wang, X.Y. Dong, et al., Chem. Eng. J. 449 (2022) 137819.
[53] J.C. Liu, J.W. Zhao, C. Streb, Y.F. Song, Coord. Chem. Rev. 471 (2022) 214734.
[54] M. Lu, M. Zhang, J. Liu, et al., J. Am. Chem. Soc. 144 (2022) 1861–1871.
[55] M. Lafuente, I. Pellejero, A. Clemente, et al., ACS Appl. Mater. Interfaces 12 (2020) 36458–36467.
[56] A.J. Bridgeman, Chem. Eur. J. 10 (2004) 2935–2941.
[57] Y.H. Han, J.J. Lan, K. Li, et al., Chem. Asian J. 17 (2022) e202200950.
[58] J.W. Jordan, J.M. Cameron, G.A. Lowe, et al., Angew. Chem. Int. Ed. 61 (2022) e202115619.
[59] X.Z. Zhang, W.J. Zhu, Z.X. Yang, et al., J. Mater. Chem. C 10 (2022) 15451–15457.
[60] D. Zhou, B.H. Han, Adv. Funct. Mater. 20 (2010) 2717–2722.
[61] J.C. Liu, J.F. Wang, Q. Han, et al., Angew. Chem. Int. Ed. 60 (2021) 11153–11157.
[62] X.Q. Huang, W.L. Cui, S. Liu, et al., Chin. Chem. Lett. 34 (2023) 107692.
[63] L.G. Gong, X.X. Qi, K. Yu, et al., J. Mater. Chem. A 8 (2020) 5709–5720.
[64] J.Y. Zhang, X.Y. Wang, G. Wang, et al., Chin. Chem. Lett. 34 (2023) 107231.
[65] G.G. Wang, T.C. Chen, C.J. Gómez–García, et al., Small 16 (2020) 2001626.
[66] Z.B. Zhang, Z.F. Li, Z.M. Dong, et al., Chin. Chem. Lett. 33 (2022) 3577–3580.
[67] J. Hu, F.F. Jia, Y.F. Song, Chem. Eng. J. 326 (2017) 273–280.
[68] M. Jiang, D.D. Zhu, H.Y. Zhang, X.B. Zhao, New J. Chem. 38 (2014) 3354–3357.